PNAS RESEARCH ARTICLE | APPLIED PHYSICAL SCIENCES

Engineering spin coherence in core-shell diamond nanocrystals

Uri Zvi[a], Denis R. Candido[b], Adam M. Weiss[c], Aidan R. Jones[d], Lingjie Chen[a,d], Iryna Golovina[c,e], Xiaofei Yu[d], Stella Wang[d], Dmitri V. Talapin[a,c,f], Michael E. Flatté[b,g], Aaron P. Esser-Kahn[a], and Peter C. Maurer[a,f,1]

Affiliations are included on p. 8.

Edited by Shanying Cui, HRL Laboratories LLC, Malibu, CA; received October 30, 2024; accepted March 31, 2025 by Editorial Board Member Evelyn L. Hu

Fluorescent diamond nanocrystals can host spin qubit sensors capable of probing the physical properties of biological systems with nanoscale spatial resolution. Sub-100 nm diamond nanosensors can readily be delivered into intact cells and even living organisms. However, applications beyond current proof-of-principle experiments require a substantial increase in sensitivity, which is limited by surface induced charge instability and electron-spin dephasing. In this work, we utilize engineered core-shell structures to achieve a drastic increase in qubit coherence times (T_2) from 1.1 to 35 μs in bare nanodiamonds to upward of 52 to 87 μs. We use electron-paramagnetic-resonance results to present a band bending model and connect silica encapsulation to the removal of deleterious mid-gap surface states that are negatively affecting the qubit's spin properties. Combined with a 1.9-fold increase in particle luminescence these advances correspond to up to two-order-of-magnitude reduction in integration time. Probing qubit dynamics at a single particle level further reveals that the noise characteristics fundamentally change from a bath with spins that rearrange their spatial configuration during the course of an experiment to a more dilute static bath. The observed results shed light on the underlying mechanisms governing fluorescence and spin properties in diamond nanocrystals and offer an effective noise mitigation strategy based on engineered core-shell structures.

quantum sensing | nanodiamonds | qubit coherence | quantum engineering | core-shell

Significance

Nitrogen-vacancy (NV) centers in diamond nanocrystals serve as powerful nanoscale quantum sensors, yet they suffer from surface-induced spin decoherence and charge instability that limit their sensitivity. This study demonstrates that an established surface modification using a core-shell design can serve as an approach to enhancing the stability and the coherence of NV centers. The core-shell design significantly increases luminescence, reduces the density of paramagnetic species, and extends NV coherence times by up to 3.5-fold. It represents a robust, scalable, and facile strategy for deploying highly sensitive quantum sensors in complex biological environments. This work provides a foundational advancement in nanoscale quantum sensing, with implications for precision diagnostics, cellular imaging, and other bioengineering applications.

NV centers in diamond nanocrystals have emerged as powerful optically detectable sensors for probing magnetic fields (1, 2), electric fields (3), and temperature (4, 5) in living systems. First applications of diamond-based sensing are emerging in neuroscience (6), developmental biology (5), cellular physiology (7, 8), and medical diagnostics (9). However, many potential applications relying on diamond nanocrystal-based sensing remain limited due to reduced NV fluorescence, caused by charge instabilities, and shortened NV T_2-times, associated with surface noise (10).

Specifically for particles with a size below 100 nm, charge and spin noise associated with the crystal's surface become a dominant factor (11). Various approaches to improving fluorescent and spin coherence in diamond micro- and nanocrystals have been pursued. Notably, these approaches include mechanical milling (12, 13) or lithographically (14) etching high-purity bulk diamond to microscale particles, which under dynamical decoupling, results in bulk-like T_2-times (see *SI Appendix*, Fig. S1 for a comparison chart). Although promising, the microscale size (hundreds of nanometers (12, 13) in the case of milling and pillar length of a few micrometers (14) in the case of lithographic etching) of these particles severely limits biological applications. Moreover, the top- down fabrication required in lithography results in a low yield, limited to tens of micrograms, which makes the processing of large quantities required for biological labeling prohibitively expensive.

Another approach toward the mitigation of surface noise relies on controlling the diamond surface termination, which on highly ordered bulk diamond surfaces, has led to a significant increase in spin coherence (15). However, in diamond nanocrystals a similar effect on coherence has yet to be observed.

Surface Passivation by Engineering Core-Shell Structures

In nanotechnology, engineered core-shell structures have been established as an effective strategy to mitigate adverse surface effects on luminescence. For example, encapsulation in a protective shell reduces surface-induced photoblinking in quantum dots (16) and nonradiative relaxation in lanthanide-doped upconverting nanoparticles (17, 18). In principle, a similar coating strategy could lead to enhanced qubit coherence by saturating dangling bonds and eliminating paramagnetic defects or charge traps located near the particle's surface (18).

Author contributions: U.Z., D.R.C., M.E.F., A.P.E.-K., and P.C.M. designed research; U.Z., D.R.C., A.M.W., A.R.J., L.C., I.G., X.Y., and S.W. performed research; I.G. and D.V.T. contributed analytic tools; U.Z. and D.R.C. analyzed data; and U.Z., D.R.C., A.P.E.-K., and P.C.M. wrote the paper.

Competing interest statement: WO 2023288108 A1–Metal-oxide shell growth on diamond for increased coherence of nitrogen-vacancy centers and improved sensing sensitivity.

This article is a PNAS Direct Submission. S.C. is a guest editor invited by the Editorial Board.

[1]To whom correspondence may be addressed. Email: pmaurer@uchicago.edu.

This article contains supporting information online at https://www.pnas.org/lookup/suppl/doi:10.1073/pnas.2422542122/-/DCSupplemental.

Published May 21, 2025.

However, extending qubit coherence in core-shell structured particles has so far remained elusive (11, 19).

In this work, we explore core-shell structures to efficiently passivate the diamond surface. Specifically, we investigate dense silica shells that have been shown to form chemically functionalizable, biocompatible coatings (20, 21). These core-shell structures result in enhanced fluorescence rate and a T_2 extension that rivals those of near-surface NVs in high-purity bulk crystals (15).

Optical Properties of Bare and Core-Shell Structured Diamond Nanocrystals. As a substrate, we use electron irradiated and thermally annealed (850 °C) carboxylated diamond nanocrystals with a reported average diameter of 40 to 45 nm and 10 to 12 NV centers per particle (22). We emphasize that particles from the same batch were used to analyze the particles before and after coating. The diamond nanocrystals were encapsulated with 18 ± 2 nm silica shells using an adapted Stöber process with tetraethyl orthosilicate (TEOS) to obtain core-shell structured particles (23), resulting in milligrams of diamond core-shell particles (*SI Appendix*, Fig. S2 and Section S1). We note that while different diamond encapsulation strategies have been developed (23–26), we chose a slight modification of the method described in ref. 23 for its high-density shells.

Transmission electron microscopy (TEM) reveals dense silica shells with homogeneous surface coating for these core-shell structures (Fig. 1*A* and *SI Appendix*, Fig. S3). Using correlative light-electron microscopy (CLEM) imaging to clearly distinguish the diamond core (*SI Appendix*, Fig. S4), we demonstrate that fluorescent bare and core-shell structures exhibit no significant difference in their core diamond size (P = 0.640). A careful examination further indicates that, for a given core size, core-shell particles exhibit a 1.9-fold increase in luminescence compared to bare particles (Fig. 1*B* and *SI Appendix*, Fig. S4 and Sections S2 and S3. See Dataset S1 for the entire dataset). Deconvolution of the fluorescence spectra of NV^0 and NV^- suggests a 20% increase in the NV^- fraction, confirming that our core-shell structures stabilize the desired negatively charged NV center (Fig. 1*C*). Previous studies (27, 28) point to the existence of deleterious diamond surface states that reduce charge stability and quench the NV fluorescence signal. Notably, our CLEM and fluorescence spectra studies suggest that silica encapsulation suppresses such surface states, as confirmed by recent X-ray absorption spectroscopy results (29). We attribute the additional increase in fluorescence to a larger photonic density of state in the silica shell compared with air (30).

Paramagnetic Defect Densities in Core-Shell Structures. We start by investigating the type and density of paramagnetic defects present in bare and core-shell structured diamond nanocrystals. Continuous wave electron paramagnetic resonance (EPR) spectroscopy on lyophilized bare and core-shell structured nanocrystals reveals the spectroscopic signatures of at least three distinct resonances (Fig. 2 *A* and *B*). One resonance can be attributed to the presence of substitutional nitrogen defects (P1 centers) identified by their characteristic hyperfine interactions with the ^{14}N nuclear spin (32). The second resonance, henceforth referred to as X-spins, has been suggested to correspond either to dangling bonds (33) or negatively charged vacancies in the near-surface region (34)—for both defects, the expected g-factor lies within the precision of our spectrometer. The remaining third resonance can be assigned to a hydrogen atom-vacancy (H1) complex (35).

Remarkably, the core-shell structures show a significant reduction of all resonances when compared to the bare diamond nanocrystals (i.e., X-spin density is reduced by 3.8×, H1 by 2.6×, and P1 by 1.8×). The depletion in X and P1 defects points toward a band-bending at the diamond–silica interface due to changes in surface potential (36). We illustrate this effect by aligning the

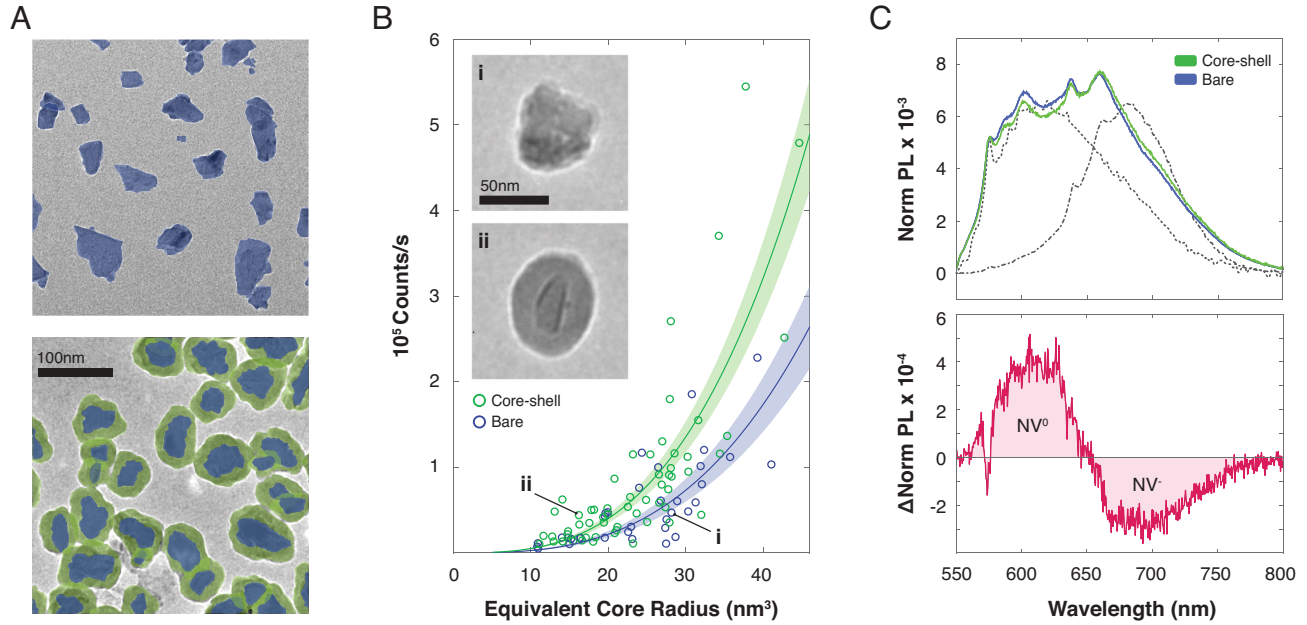

Fig. 1. Optical properties of bare and core-shell particles. (*A*) False-colored TEM of Bare (*Top*) and core-shell (*Bottom*) particles. Blue corresponds to the diamond core and green to the silica shell (for raw TEM images and size distributions see *SI Appendix*, Fig. S3). The aggregation of core-shell particles is an artifact of drying the solution on the TEM grid (*SI Appendix*). (*B*) CLEM measurements of fluorescence of core-shell (green circles) and bare (blue circles) particles as a function of their diamond core radius. Solid lines represent a fit to $y = ar^3$, where r is the core radius and a is a fit parameter. *Inset*: representative TEM of a bare (*i*) and a core-shell (*ii*) particle, marked in red on the main panel. Although these particles exhibit similar fluorescent intensity, the diamond core radius of the core-shell particle is smaller. (*C*) Normalized spectrum (*Top*) obtained from an ensemble of core-shell (green) and bare (blue) particles. Dashed black lines represent deconvolution to NV^0 (*Left*) and NV^- (*Right*) (black lines are extracted from figure 1 in ref. 31). Subtraction (lower panel) of the core-shell spectrum from bare spectrum showing a shift from NV^0 to NV^- in core-shell particles. Spectral decomposition reveals that for bare diamond, 24% of the emission originates from NV^- and for core-shell structures, 29% originates from NV^-.

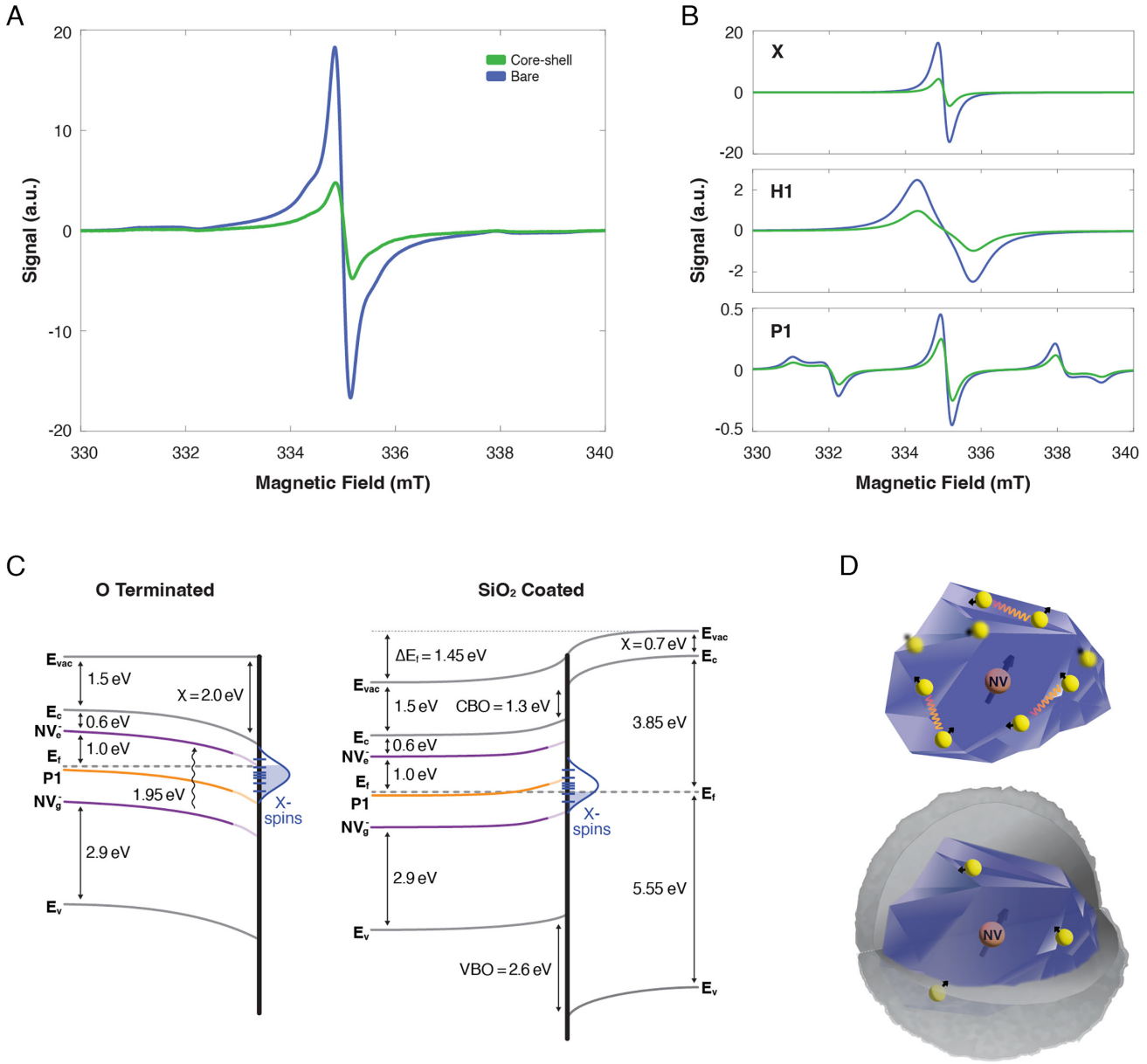

Fig. 2. EPR of paramagnetic defects in bare and core-shell particles. (*A*) Continuous wave X-band EPR (g = 2.0031 ± 0.00005) for bare (blue) and core-shell (green) diamond nanocrystals with ~70 nm core size. (*B*) Spectral deconvolution of the EPR signal into contributions from X (g = 2.0032), H1 (g = 2.0028), and P1-spins (g = 2.0026), normalized to a sample mass of 1 mg. All measurements were performed at room temperature. See methods and SI5 for details about EPR spectrum modeling. (*C*) Band energy diagram for both oxygen-terminated (*Left*) and SiO2-coated (*Right*) diamonds with corresponding affinities (χ). The model shows the corresponding spatial dependence of the Fermi level (Ef), conduction band minimum (Ec), valence band maximum (Ev), and substitutional nitrogen (P1; orange). The diamond–silica heterojunction exhibits a type 1 band alignment with an upward band bending of diamond energy levels. A conduction band offset (CBO) of 1.3 eV and a valence band offset (VBO) of 2.6 eV promote confinement of charges to the diamond, as supported by the higher fluorescence of core-shell particles. The energies and occupation of X-spins levels are also illustrated as a Gaussian near Ef, positioned within the ~1.95 eV gap between the NV center ground (NV^-) and excited (NV^-) gestates. (*D*) Schematic depiction of a bare (*Top*) and a core-shell (*Bottom*) structured diamond nanocrystal with an NV-qubit (orange) in the diamond host blue. Surface spins are indicated in yellow.

electronic structures of type Ib oxygen-terminated diamond (N doped at ~100 ppm) and amorphous silica (Fig. 2*C* and *SI Appendix*, Fig. S6 for band structure and Fig. 2*D* for a schematic representation). The reported surface electron affinity, χ_S ~ 2 eV, of oxygen-terminated bare diamond (37) leads to a downward band-bending that stabilizes P1 and X-spins (left panel). In contrast to bare diamond, silica encapsulation results in an upward band bending, which depletes P1 and X-spins without affecting the energetically lower laying NV^- charge state (right panel). In addition to the depletion of noisy paramagnetic species, the large energy barrier (~1 eV) prevents tunneling of electrons deep into the SiO_2 (38), which is expected to result in an increased charge stability during photoexcitation. We confirm our model with a band bending simulation based on a solution of the Poisson equation (*Materials and Methods* and *SI Appendix*, Fig. S7 and Section S6). The resulting band structure suggests a 3.8 nm thick P1 depletion layer at the diamond–silica interface, which translates into a 44% decrease in the number of P1 centers per nanoparticle. As supported by our band bending model, our simulation predicts that the NV^- density remains unaffected by our core-shell structures. We note that direct chemical conjugation of dangling bonds or displacement of paramagnetic species in the hydrolyzation layer by silica encapsulation complement our band-bending analysis and result in a reduction of paramagnetic spins at the surface (29, 39). We explore the

connection between reports of mid-gap states removal and our current work in the concluding discussion.

Qubit Coherence in Core-Shell Structured Particles. EPR spectroscopy provides important insights into the presence and density of paramagnetic defects in bare and core-shell particles. However, ensemble EPR spectroscopy does not account for particle heterogeneity and, at least in our case, does not possess the sensitivity to directly probe NV-qubits [NV centers have a ~100× reduced density compared to P1 centers (22)]. We overcome this challenge by selectively probing the NV spins within individual optically resolvable diamond nanocrystals. Double electron–electron resonance (DEER) measurements confirm the coupling of the NV-qubit to X-spin and P1 (*SI Appendix*, Fig. S8 and Section S7). Fig. 3*A* show the observed T_1- times for bare and core-shell diamond nanocrystals. The single quantum relaxation time (T_1^{SQ}), which describes relaxations between m_s = 0 and m_s = ±1, sharply increases from (114 ± 16) μs for uncoated particles to (379 ± 33) μs for engineered core-shell structures. However, double quantum relaxations (T_1^{DQ}), the transitions between m_s = ±1, remain unaffected by coating (Fig. 3 *A*, *Inset*). This suggests that low-frequency electronic noise is not impacted by our engineered core-shell structures.

Having established that engineered core-shell structures result in an increase in qubit T_1, we next investigate its effect on T_2. Spin Echo experiments reveal that bare and coated particles exhibit a T_2^{Echo} of (1.05 ± 0.41) μs and (1.42 ± 0.20) μs, respectively (*SI Appendix*, Fig. S9 *C* and *E*). Using Carr–Purcell–Meiboom–Gill (CPMG) dynamical decoupling (40) we extend the coherence by filtering low-frequency noise with a filter function that is centered around $\omega = \pi N/T$, where N is the number of π-pulses and T is the total precession time (40). We find that for bare nanocrystals, T_2 increases with N only up to a certain level before it saturates (*SI Appendix*, Fig. S9 *A* and *F*). Fig. 3*B* shows the maximally achievable T_2 for twelve different bare diamond particles, with some particles showing no or marginal improvement with N (blue data points). Interestingly, for core-shell structured nanoparticles (green data points) we do not observe a similar heterogeneity in T_2 and find a significant T_2 increase for all eight particles (for $N > 1{,}000$ we find an average $T_2^{CPMG} = 70 \pm 12$ μs). As a consequence core-shell structures result in an average 3.5-fold increase in qubit coherence, and a 3.2-fold decrease in particle to particle T_2 variation (i.e., the relative SD is $\frac{\sigma(T_2)}{\langle T_2 \rangle} = 0.60$ for bare and $\frac{\sigma(T_2)}{\langle T_2 \rangle} = 0.19$ for core-shell particles), as depicted by the histogram in Fig. 3 *B*, *Right*). The functional dependence of T_2 on N follows a power law, $T_2(N) = T_{2,echo}N^k$, with $k = 0.53$ for core-shell and $k = 0$ to 0.47 for bare particles. The difference in scaling suggests that the spin-bath noise in core-shell structured particles is characterized by longer correlation times compared to bare particles (40) (*SI Appendix*, Section S9).

We use CLEM measurements in a similar manner to Fig. 1*B* and confirm again that the bare and core-shell particles used for spin properties measurements have comparable diamond core diameters. Fig. 3*C* shows T_1^{SQ} (*Upper*) and max T_2 times (*Lower*) as a function of diamond core size for four bare and four core-shell particles. The alignment of confocal and TEM images for one out of the four bare (*Upper*) and core-shell (*Lower*) particles is shown in Fig. 3*D* (see *SI Appendix*, Fig. S4 and Section S3 for more details about the CLEM process). A *P*-value of 0.90 indicates that the cores of the studied bare and core-shell particles are of comparable sizes, while *P*-values of 1.31×10^{-3} and 1.85×10^{-3} confirm a significant increase in T_1 and max T_2-times, respectively. Although the original particles are nominally 40 nm in diameter (*SI Appendix*, Fig. S3), we observe that both bare and core-shell particles with measurable spin coherence possess core diameters of 70 nm. While this shift to a larger size

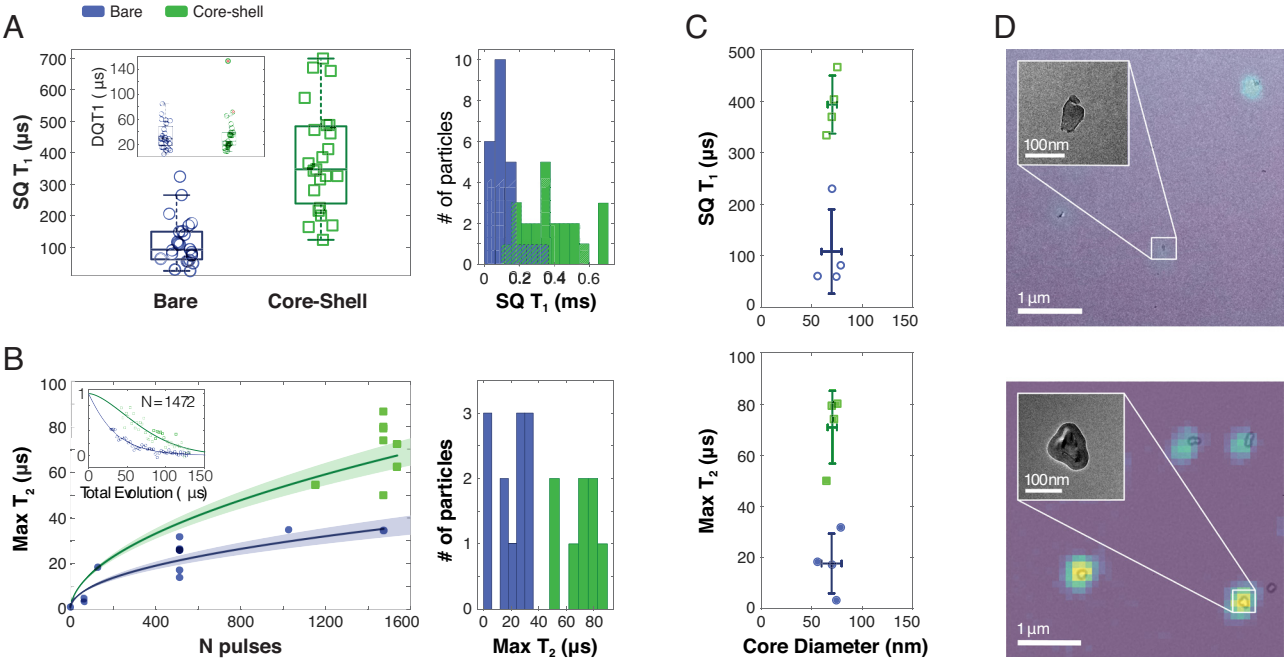

Fig. 3. Relaxation and coherence of individually resolvable diamond nanocrystals. (*A*) Single quantum relaxation measurements of bare (blue; $n = 24$) and core-shell (green; $n = 23$) particles presented as a box and whiskers plot (*Left*) and a histogram (*Right*). The *Inset* shows double quantum relaxation times of the same particles (double quantum relaxations were measured at ~6.7 G). (*B*) Maximally obtained T_2 times under CPMG dynamical decoupling of randomly selected twelve bare and eight core-shell particles presented as a function of the number of pulses applied (*Left*) and as a histogram (*Right*). Note, for some of the investigated bare diamonds T_2 does not increase with N (blue points with low N number of pulses), while for all core-shell structured particles, we observed a T_2 for $N > 1{,}000$ (*SI Appendix*, Fig. S9 and Section S9). Solid lines are fits to a power law as described in the main text. The *Inset* shows a representative coherence time trace data for one bare and one core-shell particle with $N = 1{,}472$. (*C*) Correlation of core size with T_1 (*Upper*) and max T_2 (*Lower*) for four bare and four core-shell particles. (*D*) Representative CLEM images of bare (*Upper*) and core-shell (*Lower*) particles for the data shown in *C*. *Insets* are larger magnifications of individual particles. (Scale bar, 100 nm.) See *SI Appendix*, Fig. S4 for TEM images of additional particles from each group. See Dataset S2 for full dataset.

might be related to the imaging conditions (*Materials and Methods*), it also underscores the importance of directly assessing the size of measured fluorescent particles that might be susceptible to a selection bias (*SI Appendix*, Fig. S1). We point out that different characterization techniques can result in significantly different particle size estimations. For example, atomic force microscopy (AFM) measures the particle height (12) whereas TEM measures the particle cross-section. In the case of disk-like particles, such as diamond nanocrystals produced by ball milling, AFM will, therefore, consistently underestimate the particle size when compared with TEM (41).

Quantum Mechanical Description of Bath Dynamics. The different performance under CPMG decoupling points toward a modification of the spin noise environment in our core-shell structured particles. Assuming Gaussian noise, we reconstruct the power spectra by deconvoluting the experimentally measured CPMG time traces (see ref. 40 and *Materials and Methods*), which results in the solid circles and diamonds in Fig. 4*A*. In addition to the frequency range obtained from CPMG (2 MHz to 25 MHz), we can probe high-frequency noise (~2.85 GHz) by considering the measured T_1^{SQ} spin relaxation times (*SI Appendix*, section S10). In the low-frequency regime (<3.7 MHz), we find that the noise power spectra of bare and core-shell structured nanocrystals are largely identical, while for higher frequencies the engineered core-shell structures show noise reduction of up to a factor 4.0×.

The power spectrum of a spin bath follows a Lorentzian (40). For bare particle we observe a broad power spectrum that fits a Lorentzian with short correlation times ($\tau_c \leq 1$ ns), as would be expected for a fast fluctuating surface spin bath (42). In contrast, for core-shell particles this high- frequency noise is significantly reduced, revealing a Lorentzian noise spectrum with longer correlations times [τ_c = (46 ± 11) ns], indicating a slower evolving spin bath. At low frequencies, the power spectrum deviates from a Lorentzian noise model and instead follows a 1/*f*-like scaling. The exponent (a = 1.7 and a = 1.6 for bare and core-shell particles, respectively) of this $1/f^a$-noise is extrapolated from the experimentally observed T_1^{DQ} and is in good agreement with results from near-surface NV centers in bulk diamond (43). This suggests that charge, rather than spin, fluctuations dominate the low-frequency end of the noise power spectrum (11) (*Materials and Methods* and *SI Appendix*, Fig. S10) and remain unaffected by our engineered core-shell structures.

Having gained an understanding of the noise spectral properties, we next turned our attention to the microscopic origin and quantum mechanical properties of the spin bath. In a Hahn Echo, the coherence factor $exp\ (-\chi(t))$ follows a stretched exponential with $\chi(t) \sim t^n$, where the exponent n implicitly contains information about the spin bath (44). Fig. 4*B* shows four representative examples of the time evolution of $\chi(t)$ for bare and core-shell structured particles. In the case of core-shell particles we find $n \sim 1$, which is consistent with a Markovian bath where the spatial position of each bath spin remains fixed (44) (Fig. 4*C* and *SI Appendix*, Section S11). In contrast, Hahn Echo for bare nanocrystals shows a strikingly different behavior, with n ranging from 0.4 to 2 (Fig. 4 *B* and *C*). The observation of $n < 1$ suggests that, for bare particles, the bath spins do not remain in a fixed spatial configuration, but rather change their spatial distribution over time. A similar "spin-hopping" effect is known to occur in near-surface NV centers in bulk diamond (45, 46). Therefore, the $n \sim 1$ exponent for core-shell particles suggests that the engineered shells not only reduce the paramagnetic defects density, but also reduce spin-hopping within the bath—an effect that has been plaguing diamond-based quantum sensing (45).

Discussion and Outlook

Identifying the exact microscopic origin of the surface-related paramagnetic species that limit NV coherence in diamond nanocrystals and near-surface bulk systems remains an outstanding challenge. Consistent with our EPR results, recent theoretical

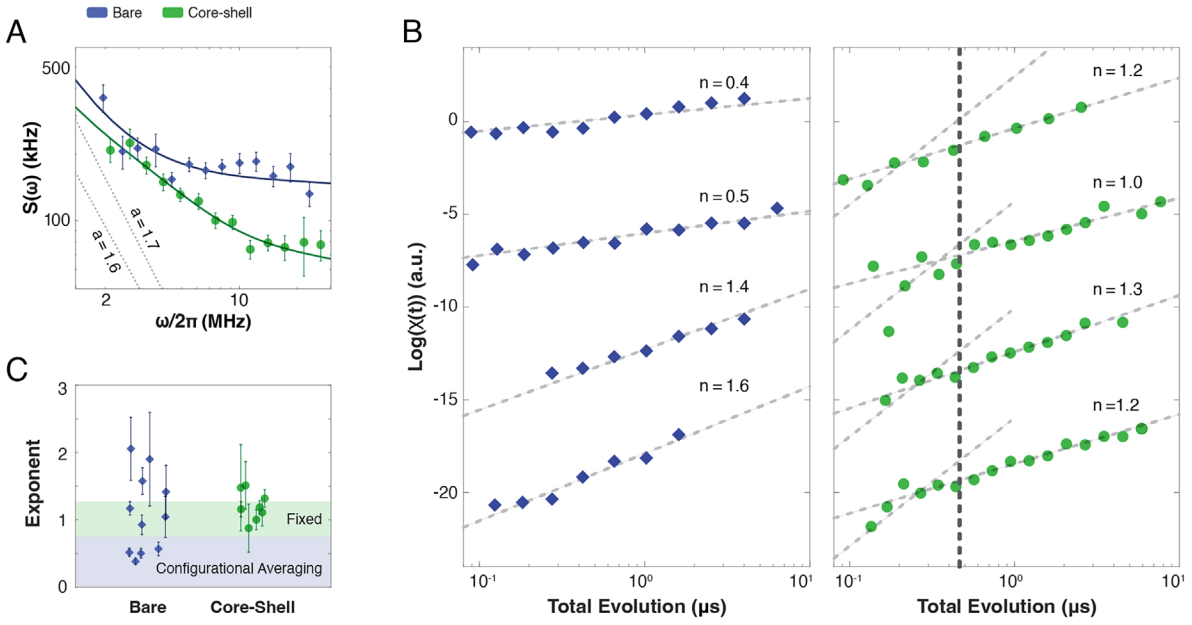

Fig. 4. Probing spin bath properties using spectral decomposition and stretching factor spectroscopy. (*A*) Spectral decomposition of CPMG data from bare (blue) and core-shell (green) particles. Gray dotted lines show fits to $1/f^a$ considering DQ data (*SI Appendix*, Fig. S10). Solid lines show fits for $1/f^a$ plus a single (for bare) or a double (for core-shell) Lorentzian, with the addition of white noise (*SI Appendix*, Fig. S10 for exact fitting details). (*B*) Four representatives bare (*Left*) and core-shell (*Right*) echo stretching factors. Gray dashed lines are exponential fits for the random walk regime (the cutoff is marked by the black dashed line). Core-shell particles also show ballistic regime fits to n = 3. (*C*) Distribution of echo stretching factors for bare (blue) and core-shell (green). Data points with $n \leq 0.75$ (blue box) can be explained by configurational averaging, while data points with $n \approx 1$ (green box) correspond to fixed spins' positions (see *SI Appendix*, Section S11 for more details).

work has proposed that surface-related sp2 and sp3 dangling bonds are a major source for NV dephasing and charge instability (28, 47). Our work points to near fermi level mid-gap surface states that are depleted during silica encapsulation. Additional insights into the nature of these surface states have been provided by XAS studies (48, 49), demonstrating mid-gap electronic states in oxygen-terminated surfaces, such as those associated with sp2 groups (~285 eV) and carbonyl groups (~287 eV). During peer review, we became aware of recent work by Sandoval et al. (29), which highlights that silica encapsulation induces hydroxylation processes that effectively eliminate mid-gap states through the formation of silyl-ether bonds (C–O–Si) and other covalent linkages. This interpretation complements our reported band bending at the diamond–silica interface and connects our results to the doubling of spin relaxation time in borane-reduced diamond nanocrystals (39). Core-shell structures suppress mid-gap surface states and hence alter the spin bath properties, leading to a significant increase in NV-qubit coherence. Moreover, the reduction of mid-gap states augments reports on low electron mobility in the silica–semiconductor interface (50) that should suppress the rate of spin hopping—an effect corroborated by the observed stretch factors in Hahn echo measurements (Fig. 4 *B* and *C*).

We demonstrate that engineered core-shell structured particles offer an efficient means to reduce heterogeneity and extend qubit coherence. In a central spin model, the qubit coherence is inversely proportional to the spin bath density (51), which puts the observed 3.5-fold increase in NV coherence in good agreement with the 3.88-fold reduction of X-defect density obtained by EPR spectroscopy. Combining our core-shell structures with dynamical decoupling we extended the NV-qubit coherence to 70 μs, which approaches the coherence times of near-surface NV centers in high-purity bulk diamond (15). Furthermore, combining optical single-particle addressability with NV-based qubit sensing reveals that engineered core-shell structures reduce qubit heterogeneity and suppress complex dynamics in spatial reconfigurations of the spin bath during the course of an experiment.

The significantly decreased heterogeneity in core-shell structured particles will be directly applicable to real-world quantum sensing experiments where large variations in T_1 and T_2, and therefore sensitivity, present a challenge to experimental reproducibility. Biophysical problems ranging from nanoscale thermometry (5) to the detection of paramagnetic species (7) to magnetometry (8) are expected to immediately benefit from such novel noise mitigation strategies. Depending on the measured particle, the observed increase in spin coherence and particle luminescence translates into a 4 to 120-fold reduction in signal integration time for the detection of a phase-coherent signal and a fivefold to 1,000-fold reduction for the detection of an incoherent signal (52). Being able to perform a measurement in a minute that otherwise would take hours can make the difference between observing and not observing an effect in biology, where measurement time is often limited.

An effective passivation of X-spins and a desired enhancement in coherence might be achieved with thinner shells down to a few nm in thickness, a mechanism that we are currently investigating. Such a reduction in shell thickness will be central for sensing applications where a minimal spatial separation between the NV-qubit sensor and the target is required. Investigating different coating protocols and chemistry may further extend coherence and at the same time provide deeper insights into the microscopic nature of the X-spins. The developed techniques can directly be extended to other qubit systems, including color centers in silicon carbide (53), lanthanide-doped nanoparticles (54), and quantum dots (19). Likewise, other diamond nanostructures where surface-induced NV dephasing is a limiting factor, such as in diamond-AFM tips and photonic structures, can benefit from a similar passivation approach. Additionally, while diamond as a material is biocompatible, diamond nanocrystals have been shown to aggregate in cellular media and even be cytotoxic (23, 26, 55–57). In contrast, silica encapsulation can improve stability and reduce cellular toxicity and inflammation (21, 23, 24, 26), suggesting that the developed coating could help reduce adverse effects on cellular processes. Finally, the complex surface chemistry of diamond nanocrystals has limited the density of functionalizable surface groups (24, 58, 59). In contrast, silica surfaces can be functionalized with high efficiency through established silanization chemistry (20). Considered together, our core-shell encapsulation will not only improve sensor sensitivity, but may also result in probes that are less invasive and more compatible with in-vivo and in-vitro studies. Our findings emphasize the potential of engineering spin coherence using fundamental nanoscience principles to significantly improve the sensitivity and applicability of real-world nanoscale quantum sensors.

Materials and Methods

Diamond Nanocrystals. 40 to 45 nm diamond nanocrystals were obtained from Adámas Nanotechnologies Inc. In brief, type 1b microcrystals are manufactured by static high-pressure, high-temperature (HPHT) synthesis and contain about 100 to 200 ppm of substitutional N. These particles are milled, irradiated with 2 to 3 MeV electrons, and annealed at 850 °C for 2 h. by Adámas Nanotechnologies Inc. (22).

Synthesis of Core-Shell Particles. The growth of Silica shells on diamond nanocrystals was performed using a sol–gel Stöber process (60) from a TEOS precursor. To ensure uniform shell growth and prevent aggregation we modified a Polyvinylpyrrolidone (PVP) based technique (23, 61) (*SI Appendix*, Figs. S2 and S3 and Section S1).

Characterization of Particles.

TEM. Bare and core-shell diamond nanocrystals were deposited on a Copper (formvar carbon film) or Silicon (Si3N4 film) grid while ensuring minimal aggregation (*SI Appendix*, Fig. S4 and Section S2). Images were taken using an FEI Tecnai G2 F30 300kV TEM.

Size analysis. Particle sizes were analyzed with the help of ImageJ (62). A 2-pixel Gaussian blur was applied before background subtraction. Thresholding was used to convert to a binary image from which the area (*A*) of an individually resolved crystal is calculated and subsequently converted to an equivalent diameter (63) (*SI Appendix*, Fig. S4 and Section S3). We analyze core-shell particles by using a two-step thresholding process to separate the darker core from the brighter shell.

CLEM Measurements. For CLEM measurements, nanocrystals were deposited on a silicon nitride TEM grid that was placed face-down on a glass coverslip with a fabricated coplanar waveguide. The sample was then placed in our home-built confocal microscope (*SI Appendix*, Section S4) for PL and coherence measurements. We note that high background signal from the silicon nitride grids was observed during PL and spin measurements, potentially leading to a preference toward larger particles. Subsequent TEM images enabled us to identify individual particles by comparing particle constellations in TEM with those obtained from confocal scans. As fiducial markers for alignment of the confocal and TEM images, we used the corners and edges of the TEM grid windows, followed by overlapping of bright PL spots to the nanocrystals' TEM pattern for fine alignment (see *SI Appendix*, Fig. S4 for more details and CLEM images for PL and coherence measurements). Once we identified the particles of interest, high-magnification images were taken.

Photoluminescence. Photoluminescence (PL) was measured for bare and core-shell particles using our home-built confocal setup (*SI Appendix*, Section S4). By drop casting a mixture of bare and core-shell particles on the same TEM grid, we were able to ensure that both particle types were measured under identical conditions (*SI Appendix*, Fig. S4). Correlation with TEM then enabled us to unambiguously identify each fluorescence spot as either a bare or a core-shell particle. A total of 93 individual particles (58 core-shell and 35 bare) were analyzed. The particle radius (see *size analysis* in *Materials and Methods* and *SI Appendix*, Section S3)

in Fig. 1*C* was fitted to ar^3, where *r* is the particle radius, and *a* is a fit parameter. We extract $a = 0.65 \pm 0.11$ for bare, and $a = 1.20 \pm 0.16$ for core-shell particles.

Spectrum Analysis. The photoluminescence (PL) spectrum of an ensemble of bare and core-shell particles with a core diameter of 70 nm was measured using Ocean Optics HR2000+ integrated into our home- built confocal microscope. We correct for variations in the particle density by normalizing the observed PL fluorescence spectrum ($PL(\lambda)$), i.e., $pl(\lambda) = PL(\lambda)/\Sigma_\lambda PL(\lambda)$. The normalized spectrum was then fitted to $pl = a[pl^{(0)}] + (1 - a)[pl^{(-)}]$, where *a* is a fit parameter with the restrictions $0 \le a \le 1$, $pl^{(0)}$ is the PL spectrum of NV^0 and $pl^{(-)}$ is that of NV^-.

EPR Measurements. EPR measurements were performed using an X-band continuous wave EPR spectrometer from Bruker (Elexsys 500) with a 100-kHz field modulation and a high-quality resonator ER 4122 SHQE. EPR spectra were collected with an incident microwave power of 2 mW, and a modulation amplitude of 0.2 mT, at room temperature. Experimental EPR spectra were decomposed into individual resonances. Fitting was done with the help of the EasySpin (64) software package which allowed us to determine spectroscopic parameters for each individual EPR signal.

Measurements were done on 70 nm particles to ensure that the average particle matches the ones that were measured for coherence. Results for bare and core-shell particles were normalized both by mass and number of particles so signals for both samples could be properly compared. See *SI Appendix*, Fig. S5 and Section S5 for details about the normalization procedure as well as results for 40 nm particles.

Electronic Band Structure. The band structures for diamond nanocrystals and amorphous Silica were derived from literature values. We considered a type 1b (~100 ppm N impurities) oxygen-terminated diamond nanocrystal with a positive electron affinity of ~2 eV and a band gap of 5.5 eV (37). The bulk conduction band, EC, lies approximately 1.5 eV below the vacuum level (36, 65) resulting in a ~0.5 eV downward band bending (66). The formation energy of P1 centers is positioned 1.7 eV below EC and only 0.1 eV below the Fermi level (36, 65, 67). The NV^- band is located 2.9 eV above the valence band (28, 68, 69). The band structure for amorphous Silica featured a large, 9.4 eV band-gap, EC that is located 0.7 eV below the vacuum level, and a fermi level that lies 5.55 eV above the valence band (70, 71). Equalization of the fermi level ($\Delta Ef = 1.45$ eV) produced the band bending for alignment at the heterojunction. See *SI Appendix*, Fig. S6 and Section S6 for more details.

Simulation. The band bending for bare and core-shell diamond nanocrystals is obtained by solving the Poisson's equation that reflects the charge density arising from electrons, holes, P1 (or ionized Nitrogen), and charged states of both vacancies and NV centers. The boundary condition for the electrostatic potential is obtained by assuming charge neutrality deep in the crystal, the formation energies and densities of defects are obtained from literature (22, 68, 72, 73), and the band bending values at the surface as extracted from the model in Fig. 2*C*. For more details on the simulation, see *SI Appendix*, Fig. S7 and Section S6.

NV-Based DEER Measurements. To confirm the coupling of these paramagnetic species to the NVs in our particles, we performed NV-based DEER experiments following the protocol described in ref. 15 and *SI Appendix*, Fig S8 and Section S7. By normalizing the contrast of a DEER measurement with respect to Hahn echo decay we remove contributions from other noise sources. Rabi frequency of the paramagnetic defects, needed for DEER free induction decay (FID), was measured using a correlation-based sequence described in ref. 74. All measurements were performed at ~205 G.

Coherence and Relaxation Measurements. All measurements were done in two different batches to ensure reproducibility. The first batch was measured using nanocrystals deposited on a #1.5 glass coverslip. The second batch was measured using nanocrystals deposited on silicon nitride TEM window grids (PELCO 15 nm or 50 nm Si3N4, for CLEM). Nanocrystals for measurement were chosen without favoring brighter emitters in the confocal imaging. We found this is crucial in order to ensure a representation of single nanocrystals with similar core sizes, as confirmed by CLEM (Fig. 3 and *SI Appendix*, Fig. S4).

T_1 measurements. SQ and DQ relaxation measurements were performed using a sequence adopted from Myers et al. (43). Setting γ as the DQ transition rate and Ω as the SQ transition rate, we can extract $T_1^{SQ} = \frac{1}{3\Omega}$ and $T_1^{DQ} = \frac{1}{\Omega + 2\gamma}$ (see *SI Appendix*, Section S8 for details). All relaxation measurements were done at low magnetic field (~6.7G) using 24 bare and 23 core-shell particles.

T_2 measurements. Coherence measurements were performed using Hahn-Echo and CPMG sequences illustrated in *SI Appendix*, Fig. S9 *A*, *Inset*. Randomly selected bare ($n = 12$) and core-shell ($n = 8$) diamond nanocrystals from two different batches (glass and silicon nitride grids) were measured for SQ and DQ relaxation times at low fields. The external magnetic field was then aligned to ~185 G for T_2 measurements starting with $N = 1$ (echo). T_2 was measured with an increasing number of dynamical decoupling pulses up to $N > 1{,}000$ or saturation (*SI Appendix*, Section S9). The max T_2 times and corresponding *N* pulses are plotted in Fig. 3*B*. *SI Appendix*, Fig. S9 shows the CPMG data collected from all the particles for T_2 echo and T_2 max.

T_2 fitting. Coherence data, $C(t)$, was fitted to a stretched exponential decay of the form $C(t) = ae^{-\chi(t)}$, where $\chi(t) = (t/T_2)^n$, and *a*, T_2, and *n* are fit parameters. To account for pulse evolution time, we set the initial time, t_0, to be equal to the total time of π pulses, such that $t_0 = Nt\pi$ (see *SI Appendix*, Fig. S9*B* and Section S9 for a numerical simulation validating this protocol). To account for pulse errors, we force the fitting parameter *a* to be monotonous decreasing in *N*. It is important to note that we are using *n* as a fitting parameter and not based on a model. Fixing $n = 3$, as would be the case of a ballistic phase evolution in a fixed spin configuration under dynamical decoupling, would significantly overestimate T_2.

Noise Spectral Density.

Theory. The coherence of a qubit is described by $C(t) = exp[-\chi(t)]$, where *t* is the total free precession time. Under CMPG decoupling with *N* π-pulses, $\chi(t)$ is given by $\chi(t) = -\frac{1}{2}\int_0^\infty \frac{d\omega}{2\pi} S(\omega)|\lambda(\omega, t)|^2$, where $|\lambda(\omega, t)|^2$ is the filtering function (75, 76). For $N \gg 1$, the filtering function presents a primary peak at $\omega = \omega_0 = N\pi/t$, yielding $C(t) \approx exp[-S(\omega_0)t]$ (*SI Appendix*, Section S11). Accordingly, measuring the coherence data for different *N* allows us to extract the spectral noise density at different frequencies, ω_0. This method is applied for both bare and coated diamonds, with corresponding $S(\omega)$ shown in Fig. 4*A*. We emphasize, however, that this method assumes linear dependence of $\chi(t)$ with respect to *t*.

Estimating $\chi(t)$ from experimental results. To ensure the condition $N \gg 1$ applies, we limit our analysis to CPMG experiments with $N > 64$. Experimentally obtained CPMG time traces (Fig. 3 *B*, *Inset* and *SI Appendix*, Fig. S9) were normalized and data points larger than 1 and smaller than 0 were discarded. The spectral density was extracted from these data using the approximation $\chi(t) = tS(\omega)/\pi$. The spectrum was binned into 14 logarithmic bins and plotted in Fig. 4*A*. See *SI Appendix*, Fig. S10 for data before binning.

Plotting DQ, CPMG, and SQ on the same scale. The DQ and SQ relaxation measurements (CPMG dephasing and SQ relaxation) are sensitive to different noise sources, i.e., DQ relaxation is sensitive to transverse electric fields at frequencies of 18.8 MHz whereas SQ relaxation is sensitive to transverse magnetic at 2.87 GHz and parallel electric fields. To compare QD and SQ relaxation measurements with our noise spectroscopy we follow the procedure described in ref. 43. See *SI Appendix*, Section S10 for more details.

Fitting. Using our measured CPMG and DQ data we can now fit a model for the noise spectrum. We follow a modified version of the procedure described in ref. 43.

The noise spectrum of a spin bath is expected to follow a Lorentzian with the generic form:

$$S(\omega) = \Sigma_k \left(\frac{\Delta_k^2 \tau_{c,k}}{\pi\left(1 + (\omega\tau_{c,k})^2\right)} \right), \qquad [1]$$

where Δk and $\tau_c k$ are the coupling strength and bath correlation time, respectively. The power spectrum corresponding to electric noise is expected to be described by $1/f^a$-noise (11, 15, 43, 77, 78).

The full fitting function for the combined noise is then given by

$$S(\omega) = \Sigma_k \left(\frac{\Delta_k^2 \tau_{c,k}}{\pi\left(1 + \left(\omega\tau_{c,k}\right)^2\right)} \right) + \frac{\Delta_e}{\omega^a}, \qquad [2]$$

$S_{DQ}(\omega) = \gamma(\omega)$ was obtained as discussed in the *T1 measurements and fitting* section of the methods. The two other parameters, Δ_e and *a*, are related to each other, such that, $\Delta = S_{DQ}(\omega_{DQ}) \times \omega^a{}_{DQ}$, where *a* is a fit parameter. The fitting process and results are illustrated in *SI Appendix*, Fig. S10.

Echo exponent analysis. A detailed derivation of the functional form of the exponent of the coherence factor can be found in *SI Appendix*, Section S11. The obtained stretching factor is the result of Ising interaction between the NV and a D-dimensional fluctuating spin bath (42, 45, 46, 77, 79).

In the following, we consider two separate scenarios:

First, we consider a Lorentzian spin bath where the spin position remains fixed in space. The stretching factor then takes the functional dependency:

$$\chi(t) \propto \begin{cases} t^3 & t \ll \tau_c \\ t & t \gg \tau_c \end{cases},$$

Second, we consider a Lorentzian spin bath where the spin position does not remain fixed and moved over time. Such a scenario is expected if paramagnetic centers of the bath can be ionized under laser excitation. The resulting stretching factor is then given by

$$\chi(t) \propto \begin{cases} t^{3D/2\alpha} & t \ll \tau_c \\ t^{D/2\alpha} & t \gg \tau_c \end{cases},$$

where D is the spatial dimensionality of the fluctuators and α is the interaction's scaling with distance ($\alpha = 3$ for dipole interactions and 2 for point-like charge interactions). Note, in our analysis, we consider both scenarios.

Fitting and plotting χ(t) time trace plots. A transition from the ballistic to the random walk regime occurs at τC, and leads to a double exponential decay for the echo signals. However, in a system with short correlation times, as is the case in our diamond nanocrystals (Fig. 4*A* and *SI Appendix*, Fig. S10), we would expect to be primarily in the random walk regime. This prevents us from using our data for an accurate fitting in the ballistic regime. To ensure analysis within the random walk regime we only consider evolution times larger than $10\tau C$, which allows us to fit this truncated data to a single exponential. The bare and core-shell echo time traces were plotted (Fig. 4*C* and *SI Appendix*, Fig. S11) using the identity $Log(\chi(t)) = Log(-Log(C(t))$. For core-shell particles in the ballistic regime, we also plotted guide to the eye $\chi(t) = \left(\frac{t}{T_2}\right)^3$ as a guide of the eye.

Statistics. All error bars represent SE unless otherwise noted. T_1 relaxation plot in Fig. 3*A* is illustrated using a box and whisker diagram showing the minimum, lower quarter (25th percentile), median, upper quarter (75th percentile), and maximum points of the given data. Outliers are marked with a red + and correspond to points that are more than $q_3 + 1.5(q_3 - q_1)$ or less than $q_1 - 1.5(q_3 - q_1)$ where q_1 and q_3 are the 25th and 75th percentiles of the sample data, respectively. A *t*-test for the bare ($n = 24$) and core-shell ($n = 23$) T_1 datasets (Fig. 3*A*) resulted in $P = 8.5 \times 10^{-8}$. A t-test for the bare ($n = 11$) and core-shell ($n = 8$) T_2-echo datasets (*SI Appendix*, Figs. S9 and S10) resulted in $P = 0.03$. A t-test for the bare ($n = 12$) and core-shell ($n = 8$) T_2 max datasets (Fig. 3*B*) resulted in $P = 4.6 \times 10^{-7}$. All analyses were done using two tails unequal variance *t*-tests.

Data, Materials, and Software Availability. All study data are included in the article and/or supporting information.

ACKNOWLEDGMENTS. We thank Michelle Klosinski for significant contributions to the artwork of the figures; Ania Jayich and Shimon Kolkowitz for insights related to surface charge noise; Nathalie de Leon, Nazar Delegan, Joseph Heremans, Olga Shenderova, and Alexander Zaitsev for discussions on surface terminations; Mouzhe Xie for help on XPS; and Susumu Takahashi and Karoly Kolczer for discussions on EPR. U.Z., and P.C.M. acknowledge financial support from the NSF Grant No. OMA-1936118 and NSF QuBBE QLCI (NSF OMA- 2121044). DEER measurements were performed by X.Y. and S.W. with support from US DOE, Basic Energy Sciences, Division of Chemical Sciences, Geosciences, and Biosciences, though ANL under Contract No. DE-AC02- 06CH11357. D.R.C. and M.E.F. were supported as part of the Center for Molecular Quantum Transduction (CMQT), an Energy Frontier Research Center funded by the U.S. Department of Energy, Office of Science, Basic Energy Sciences under Award No. DE-SC0021314. I.G. and D.V.T. acknowledge support by the NSF under Grant DMR-2019444 (IMOD and NSF-STC). We acknowledge the use of the Pritzker Nanofabrication Facility at the University of Chicago (NSF ECCS-2025633), the University of Chicago Materials Research Science and Engineering Center (DMR-2011854), as well as the assistance of Yimei Chen, Dr. Jotham Austin, and Dr. Tera Lavoie from The University of Chicago Advanced Electron Microscopy Core Facility (RRID:SCR_019198). EPR measurements were performed at the Center for Nanoscale Materials, a U.S. Department of Energy Office of Science User Facility, supported by the U.S. DOE, Office of Basic Energy Sciences, under Contract No. DE-AC02- 06CH11357. The XPS and Raman spectroscopy made use of the EPIC, Keck-II, and/or SPID facility(ies) of Northwestern University's NUANCE Center, which has received support from the Soft and Hybrid Nanotechnology Experimental (SHyNE) Resource (NSF ECCS-1542205); the MRSEC program (NSF DMR-1121262) at the Materials Research Center; the International Institute for Nanotechnology (IIN); the Keck Foundation; and the State of Illinois, through the IIN.

Author affiliations: [a]Pritzker School of Molecular Engineering, University of Chicago, Chicago, IL 60637; [b]Department of Physics and Astronomy, University of Iowa, Iowa City, IA 52242; [c]The Department of Chemistry, University of Chicago, Chicago, IL 60637; [d]The Department of Physics, University of Chicago, Chicago, IL 60637; [e]The Laboratory for Research on the Structure of Matter, University of Pennsylvania, Philadelphia, PA 19104; [f]Center for Molecular Engineering and Materials Science Division, Argonne National Laboratory, Lemont, IL 60439; and [g]Department of Applied Physics, Eindhoven University of Technology, Eindhoven 5600 MB, The Netherlands

1. J. R. Maze *et al.*, Nanoscale magnetic sensing with an individual electronic spin in diamond. *Nature* **455**, 644–647 (2008).
2. G. Balasubramanian *et al.*, Nanoscale imaging magnetometry with diamond spins under ambient conditions. *Nature* **455**, 648–651 (2008).
3. F. Dolde *et al.*, Electric-field sensing using single diamond spins. *Nat. Phys.* **7**, 459–463 (2011).
4. G. Kucsko *et al.*, Nanometre-scale thermometry in a living cell. *Nature* **500**, 54–58 (2013).
5. J. Choi *et al.*, Probing and manipulating embryogenesis via nanoscale thermometry and temperature control. *Proc. Natl. Acad. Sci. U.S.A.* **117**, 14636–14641 (2020).
6. Y. G. Ermakova *et al.*, Thermogenetic neurostimulation with single-cell resolution. *Nat. Commun.* **8**, 15362 (2017).
7. L. Nie *et al.*, Quantum monitoring of cellular metabolic activities in single mitochondria. *Sci. Adv.* **7**, eabf0573 (2021).
8. D. L. Sage *et al.*, Optical magnetic imaging of living cells. *Nature* **496**, 486–489 (2013).
9. B. S. Miller *et al.*, Spin-enhanced nanodiamond biosensing for ultrasensitive diagnostics. *Nature* **587**, 588–593 (2020).
10. J. Tisler *et al.*, Fluorescence and spin properties of defects in single-digit nanodiamonds. *ACS Nano* **3**, 1959–1965 (2009).
11. A. Gardill, M. C. Cambria, S. Kolkowitz, Fast relaxation on qutrit transitions of nitrogen- vacancy centers in nanodiamonds. *Phys. Rev. Appl.* **13**, 034010 (2020).
12. H. S. Knowles, D. M. Kara, M. Atatüre, Observing bulk diamond spin coherence in high-purity nanodiamonds. *Nat. Mater.* **13**, 21–25 (2014).
13. B. D. Wood *et al.*, Long spin coherence times of nitrogen vacancy centers in milled nanodiamonds. *Phys. Rev. B* **105**, 205401 (2022).
14. P. Andrich *et al.*, Engineered micro- and nanoscale diamonds as mobile probes for high- resolution sensing in fluid. *Nano Lett.* **14**, 4959–4964 (2014).
15. S. Sangtawesin *et al.*, Origins of diamond surface noise probed by correlating single-spin measurements with surface spectroscopy. *Phys. Rev. X* **9**, 031052 (2019).
16. M. Nirmal *et al.*, Fluorescence intermittency in single cadmium selenide nanocrystals. *Nature* **383**, 802–804 (1996).
17. D. J. Gargas *et al.*, Engineering bright sub-10-nm upconverting nanocrystals for single-molecule imaging. *Nat. Nanotechnol.* **9**, 300–305 (2014).
18. F. Wang, J. Wang, X. Liu, Direct evidence of a surface quenching effect on size-dependent luminescence of upconversion nanoparticles. *Angew. Chem. Int. Ed Engl.* **49**, 7456–7460 (2010).
19. J. A. Gupta, D. D. Awschalom, X. Peng, A. P. Alivisatos, Spin coherence in semiconductor quantum dots. *Phys. Rev. B Condens. Matter* **59**, R10421–R10424 (1999).
20. P. Singh, S. Srivastava, S. K. Singh, Nanosilica: Recent progress in synthesis, functionalization, biocompatibility, and biomedical applications. *ACS Biomater. Sci. Eng.* **5**, 4882–4898 (2019).
21. B. A. Moser, R. C. Steinhardt, A. P. Esser-Kahn, Surface coating of nanoparticles reduces background inflammatory activity while increasing particle uptake and delivery. *ACS Biomater. Sci. Eng.* **3**, 206–213 (2017).
22. O. A. Shenderova *et al.*, Review Article: Synthesis, properties, and applications of fluorescent diamond particles. *J. Vac. Sci. Technol. B* **37**, 030802 (2019).
23. I. Rehor *et al.*, Fluorescent nanodiamonds embedded in biocompatible translucent shells. *Small* **10**, 1106–1115 (2014).
24. A. Bumb, S. K. Sarkar, N. Billington, M. W. Brechbiel, K. C. Neuman, Silica encapsulation of fluorescent nanodiamonds for colloidal stability and facile surface functionalization. *J. Am. Chem. Soc.* **135**, 7815–7818 (2013).
25. E. von Haartman *et al.*, Core-shell designs of photoluminescent nanodiamonds with porous silica coatings for bioimaging and drug delivery I: Fabrication. *J. Mater. Chem. B Mater. Biol. Med.* **1**, 2358–2366 (2013).
26. Z. Chu *et al.*, Unambiguous observation of shape effects on cellular fate of nanoparticles. *Sci. Rep.* **4**, 4495 (2014).
27. M. Kaviani *et al.*, Proper surface termination for luminescent near-surface NV centers in diamond. *Nano Lett.* **14**, 4772–4777 (2014).

28. A. Stacey *et al.*, Evidence for primal sp^2 defects at the diamond surface: Candidates for electron trapping and noise sources. *Adv. Mater. Interfaces* **6**, 1801449 (2019).
29. P. J. Sandoval *et al.*, Quantum diamonds at the beach: Chemical insights into silica growth on nanoscale Diamond using multimodal characterization and simulation. *ACS Nano.* **3**, 462–474 (2023).
30. A. Khalid *et al.*, Lifetime reduction and enhanced emission of single photon color centers in nanodiamond via surrounding refractive index modification. *Sci. Rep.* **5**, 11179 (2015).
31. L. Rondin *et al.*, Surface-induced charge state conversion of nitrogen-vacancy defects in nanodiamonds. *Phys. Rev. B* **82**, 115449 (2010).
32. J. H. N. Loubser, J. A. van Wyk, Electron spin resonance in the study of diamond. *Rep. Prog. Phys.* **41**, 1201 (1978).
33. A. I. Shames *et al.*, Defects and impurities in nanodiamonds: EPR, NMR and TEM study. *J. Phys. Chem. Solids* **63**, 1993–2001 (2002).
34. Z. Peng, T. Biktagirov, F. H. Cho, U. Gerstmann, S. Takahashi, Investigation of near-surface defects of nanodiamonds by high-frequency EPR and DFT calculation. *J. Chem. Phys.* **150**, 134702 (2019).
35. A. V. Fionov *et al.*, Paramagnetic centers in detonation nanodiamonds studied by CW and pulse EPR. *Chem. Phys. Lett.* **493**, 319–322 (2010).
36. L. Diederich, O. M. Küttel, P. Aebi, L. Schlapbach, Electron affinity and work function of differently oriented and doped diamond surfaces determined by photoelectron spectroscopy. *Surf. Sci.* **418**, 219–239 (1998).
37. E. Janitz *et al.*, Diamond surface engineering for molecular sensing with nitrogen-vacancy centers. *J. Mater. Chem.* **10**, 13533–13569 (2022).
38. J. Cañas *et al.*, High-quality SiO_2/O-terminated diamond interface: Band-gap, band-offset and interfacial chemistry. *Nanomaterials (Basel)* **12** (2022).
39. R. G. Ryan *et al.*, Impact of surface functionalization on the quantum coherence of nitrogen-vacancy centers in nanodiamonds. *ACS Appl. Mater. Interfaces* **10**, 13143–13149 (2018).
40. N. Bar-Gill *et al.*, Suppression of spin-bath dynamics for improved coherence of multi-spin- qubit systems. *Nat. Commun.* **3**, 858 (2012).
41. N. W. Song, K. M. Park, I.-H. Lee, H. Huh, Uncertainty estimation of nanoparticle size distribution from a finite number of data obtained by microscopic analysis. *Metrologia* **46**, 480 (2009).
42. T. Rosskopf *et al.*, Investigation of surface magnetic noise by shallow spins in diamond. *Phys. Rev. Lett.* **112**, 147602 (2014).
43. B. A. Myers, A. Ariyaratne, A. C. B. Jayich, Double-quantum spin-relaxation limits to coherence of near-surface nitrogen-vacancy centers. *Phys. Rev. Lett.* **118**, 197201 (2017).
44. Z.-H. Wang, S. Takahashi, Spin decoherence and electron spin bath noise of a nitrogen- vacancy center in diamond. *Phys. Rev. B* **87**, 115122 (2013).
45. B. L. Dwyer *et al.*, Probing spin dynamics on diamond surfaces using a single quantum sensor. *PRX Quantum* **3**, 040328 (2022).
46. E. J. Davis *et al.*, Probing many-body dynamics in a two-dimensional dipolar spin ensemble. *Nat. Phys.* **19**, 836–844 (2021).
47. J.-P. Chou, P. Udvarhelyi, N. P. de Leon, A. Gali, Ab initio study of (100) diamond surface spins. *Phys. Rev. Appl.* **20**, 014040 (2021).
48. A. Wolcott *et al.*, Surface structure of aerobically oxidized Diamond nanocrystals. *J. Phys. Chem. C* **118**, 26695–26702 (2014).
49. A. Chemin *et al.*, Surface-mediated charge transfer of photogenerated carriers in Diamond. *Small Methods* **7**, e2300423 (2023).
50. L.-L. Chua *et al.*, General observation of n-type field-effect behaviour in organic semiconductors. *Nature* **434**, 194–199 (2005).
51. G. Balasubramanian *et al.*, Ultralong spin coherence time in isotopically engineered diamond. *Nat. Mater.* **8**, 383–387 (2009).
52. C. L. Degen, F. Reinhard, P. Cappellaro, Quantum sensing. *Rev. Mod. Phys.* **89**, 035002 (2017).
53. M. Radulaski *et al.*, Scalable quantum photonics with single color centers in silicon carbide. *Nano Lett.* **17**, 1782–1786 (2017).
54. A. D. Ostrowski *et al.*, Controlled synthesis and single-particle imaging of bright, sub-10 nm lanthanide-doped upconverting nanocrystals. *ACS Nano* **6**, 2686–2692 (2012).
55. Y. Xing *et al.*, DNA damage in embryonic stem cells caused by nanodiamonds. *ACS Nano* **5**, 2376–2384 (2011).
56. V. Thomas, B. A. Halloran, N. Ambalavanan, S. A. Catledge, Y. K. Vohra, In vitro studies on the effect of particle size on macrophage responses to nanodiamond wear debris. *Acta Biomater.* **8**, 1939–1947 (2012).
57. X. Zhang *et al.*, Biodistribution and toxicity of nanodiamonds in mice after intratracheal instillation. *Toxicol. Lett.* **198**, 237–243 (2010).
58. D. H. Jariwala, D. Patel, S. Wairkar, Surface functionalization of nanodiamonds for biomedical applications. *Mater. Sci. Eng. C* **113**, 110996 (2020).
59. A. Krueger, "Current issues and challenges in surface chemistry of nanodiamonds" in *Nanodiamonds*, J.-C. Arnault, Ed. (Elsevier, 2017), pp. 183–242.
60. W. Stöber, A. Fink, E. Bohn, Controlled growth of monodisperse silica spheres in the micron size range. *J. Colloid Interface Sci.* **26**, 62–69 (1968).
61. C. Graf, D. L. J. Vossen, A. Imhof, A. van Blaaderen, A general method to coat colloidal particles with silica. *Langmuir* **19**, 6693–6700 (2003).
62. C. A. Schneider, W. S. Rasband, K. W. Eliceiri, NIH Image to ImageJ: 25 years of image analysis. *Nat. Methods.* **9**, 671–675 (2012).
63. I. Rehor, P. Cigler, Precise estimation of HPHT nanodiamond size distribution based on transmission electron microscopy image analysis. *Diam. Relat. Mater.* **46**, 21–24 (2014).
64. S. Stoll, A. Schweiger, EasySpin, a comprehensive software package for spectral simulation and analysis in EPR. *J. Magn. Reson.* **178**, 42–55 (2006).
65. L. Diederich *et al.*, Photoelectron emission from nitrogen- and boron-doped diamond (100) surfaces. *Surf. Sci.* **417**, 41–52 (1998).
66. V. Petráková *et al.*, Luminescence of nanodiamond driven by atomic functionalization: Towards novel detection principles. *Adv. Funct. Mater.* **22**, 812–819 (2012).
67. R. G. Farrer, On the substitutional nitrogen donor in diamond. *Solid State Commun.* **7**, 685–688 (1969).
68. P. Deák, B. Aradi, M. Kaviani, T. Frauenheim, A. Gali, Formation of NV centers in diamond: A theoretical study based on calculated transitions and migration of nitrogen and vacancy related defects. *Phys. Rev. B* **89**, 075203 (2014).
69. K. Xu *et al.*, Photoinduced charge injection from shallow point defects in Diamond into water. *ACS Appl. Mater. Interfaces* **16**, 37226–37233 (2024).
70. V. Astašauskas *et al.*, Optical and electronic properties of amorphous silicon dioxide by single and double electron spectroscopy. *J. Electron Spectrosc. Relat. Phenom.* **241**, 146829 (2020).
71. D. A. Stephenson, N. J. Binkowski, X-ray photoelectron spectroscopy of silica in theory and experiment. *J. Non-Cryst. Solids* **22**, 399–421 (1976).
72. D. A. Broadway *et al.*, Spatial mapping of band bending in semiconductor devices using in situ quantum sensors. *Nature Electron.* **1**, 502–507 (2018).
73. N. Nunn *et al.*, Electron irradiation–induced paramagnetic and fluorescent defects in type Ib high pressure–high temperature microcrystalline diamonds and their evolution upon annealing. *J. Appl. Phys.* **132**, 075106 (2022).
74. A. O. Sushkov *et al.*, Magnetic resonance detection of individual proton spins using quantum reporters. *Phys. Rev. Lett.* **113**, 197601 (2014).
75. G. S. Uhrig, Keeping a quantum bit alive by optimized pi-pulse sequences. *Phys. Rev. Lett.* **98**, 100504 (2007).
76. W. Yang, W.-L. Ma, R.-B. Liu, Quantum many-body theory for electron spin decoherence in nanoscale nuclear spin baths. *Rep. Prog. Phys.* **80**, 016001 (2017).
77. D. R. Candido, M. E. Flatté, Interplay between charge and spin noise in the near-surface theory of decoherence and relaxation of C_3v symmetry qutrit spin-1 centers. *Phys. Rev. B* **110**, 024419 (2024).
78. D. R. Candido, M. E. Flatté, Theory of spin center sensing of diffusion and other surface electric dynamics. *Phys. Rev. B.* **110**, 174450 (2024).
79. E. B. Fel'dman, S. Lacelle, Configurational averaging of dipolar interactions in magnetically diluted spin networks. *J. Chem. Phys.* **104**, 2000–2009 (1996).